Experimental monitoring of CO2 hydrate slurry crystallization by heat flux rate determination in a jacketed reactor

Véronique Osswald, Pascal Clain, L. Fournaison, Anthony Delahaye

▶ To cite this version:

> Véronique Osswald, Pascal Clain, L. Fournaison, Anthony Delahaye. Experimental monitoring of CO2 hydrate slurry crystallization by heat flux rate determination in a jacketed reactor. International Journal of Heat and Mass Transfer, 2023, 217, pp.124665. ⟨10.1016/j.ijheatmasstransfer.2023.124665⟩. ⟨hal-04211411⟩

HAL Id: hal-04211411
https://hal.inrae.fr/hal-04211411v1

Submitted on 20 Sep 2023

Experimental monitoring of CO_2 hydrate slurry crystallization by heat flux rate determination in a jacketed reactor

Veronique Osswald[a], Pascal Clain[b, a], Laurence Fournaison[a], Anthony Delahaye[a]

[a] Université Paris-Saclay, INRAE, FRISE, 92761, Antony, France.

[b] Leonard de Vinci Pôle Universitaire, Research Center, 12 avenue Léonard de Vinci, 92916, Paris La Défense, France.

HIGHLIGHTS

- Monitoring of CO_2 hydrate formation kinetics in reactor by heat balance
- Heat flux measurement by thermopile on the reactor shell
- Highlighting the impact of stirring mobile and speed on hydrates formation kinetics
- Experimental validation by comparison with a mass balance

ABSTRACT

CO_2 hydrate slurries are promising phase change materials for secondary refrigeration applications. However, the difficulty of experimentally evaluating the crystallization kinetic of slurries limits their industrial use. Hydrate crystallization kinetics monitoring performs traditionally by a reactor mass balance. However, this method requires assumptions on CO_2 liquid phase concentration and the hydration number. This work outlines the development of a specific method to determine kinetics thanks to the direct measure of heat flow through the reactor jacket and its evaluation compared with the mass balance method. The results of each method are then obtained by testing the two kinetic parameters of stirring speed and propeller type. The final hydrate mass fractions obtained with both methods are in good agreement, but the kinetic obtained by the mass balance method is faster than by the heat balance method.

Keywords: Carbon dioxide hydrate; kinetic; heat transfer; heat and mass balances; thermopile

1. INTRODUCTION

CO_2 hydrates are interesting phase change materials [1] due to their high energy density for secondary refrigeration systems [2, 3]. This property allows them to store large quantities of cold thermal energy and for slurries to be used as a cold-energy transport medium from production to use places [4]. CO_2 hydrate slurries are composed of a liquid carrier phase, mainly water in the case of aqueous slurries, and a suspension of CO_2 hydrates, solid crystals defined as a lattice of water molecules trapping CO_2 molecules [5]. Thermodynamic properties of CO_2 hydrate are well-established slurries [6, 7], including mixed semi-clathrate of CO_2 and ammonium salts [8] or other promoters. Less research has been applied towards both energetic properties [9-14] and rheological properties [15-21]. Hydrates slurries are designed to have a high hydrate formation rate [11] and prevent agglomeration within the slurry [22]. A more accurate understanding of the crystallization mechanism of CO_2 hydrates is essential to effectively evaluate and improve the overall process efficiency [23].

Gas hydrate formation follows the classical theory of crystallization, which considers an initial nucleation stage followed by a growth stage [24]. During the nucleation or birth stage, a solution remains in conditions that are thermodynamically favorable to the existence of hydrates but without stable hydrate crystals, known as the supersaturated state. The work on methane hydrate of Vysniauskas, Bishnoi, and Englezos [25-27] highlighted that local methane concentration in solution at crystallization point was higher than predicted by liquid-vapor equilibrium. During this nucleation stage, nuclei or germs, which appear and grow, are unstable and disappear until they reach a critical size. The transition between the nucleation and growth stage appears when at least one nuclei reaches the critical size and still grows. Five physical phenomena take place simultaneously during the crystal growth stage: the CO_2 absorption from the gas phase to the liquid phase, the diffusion of the CO_2 molecule from the liquid phase to the hydrate particle surface, the incorporation of CO_2 and H_2O molecules in the hydrate crystal lattice, the heat released from crystal lattice to the bulk of the liquid phase (because crystallization is an exothermic phenomenon), and the heat exchanged with reactor environment [28].

Gas hydrate formation can be studied at a laboratory scale in stirred reactors from a few hundred milliliters to a few liters. Classical approaches to characterize gas hydrate conversion are based on the determination of (i) the amount of gas in the reactor as a function of time, (ii) CO_2 concentration in the liquid phase, and (iii) the hydration number (i.e., the CO_2 mole number per H_2O mole number present in the crystal structure). The amount of gas is obtained by either CO_2 flow measurement for semi-batch reactors [25, 29] or pressure and temperature measurement for batch reactors [30, 31]. Those experimental models involve assumptions to estimate the hydration number based on literature data from PVT approaches [2] or structural approaches such as X-Ray [32] or Raman spectroscopy [33] and the concentration of CO_2 in a liquid phase, generally taken at the liquid-vapor equilibrium [3]. To address these assumptions, some studies have been conducted using on-line probes to monitor hydrate crystals formed or concentration in the liquid phase [34-38]. Recently, Boufares, et al. [34] studied hydrate formation kinetics in a semi-batch stirred reactor (few hundred milliliters) while monitoring CO_2 concentration in real-time and in situ by infrared spectroscopy. These results highlighted that gas-liquid transfer could be the limiting factor at this scale under moderate stirring, with CO_2 hydrates able to absorb a significant quantity of CO_2 (playing the role of a CO_2 sponge). The consequence of these phenomena is the establishment of a "local" liquid-hydrate equilibrium.

Calorimetric measurements allow the ability to understand phenomena (i.e., reaction mechanism, change of state) [39, 40] and to follow the kinetics of a broad range of types of chemical, polymerization, or crystallization reactions [41, 42] performed in dedicated measuring cells. A limitation of these methods is the small volume of the measuring cells (mL to dL). Extrapolating these methods to bigger scales, such as multi-liter jacketed reactors, is challenging. However, reaction calorimeter development has increased recently, facilitated by a few hundred milliliters reactors equipped with a cooling jacket and a stirring system. Reaction calorimetry methods assume that the heat released or absorbed by the transformation exchanges instantaneously and entirely with the environment through the reactor wall. This assumption is strong and holds true only for well-insulated devices equipped with a cooling-jacket covering the entire height of the reactor. Additionally, the nature of the stirred homogeneous (bulk) or heterogeneous (porous) medium also plays a significant role, as demonstrated by the studies of Yin, et al. [43]. Generally, in this type of device, the temperature of the reactor content (Tr) is controlled by varying the temperature of the cooling/heating liquid inside a jacket (Tj). The heat-flow rate from the reactor content through the wall into the cooling/heating liquid is determined:

- by measuring the temperature difference on both sides of the reactor's wall, i.e., between reactor content and cooling liquid. To convert this temperature signal into a heat-flow signal, a heat-transfer coefficient has to be determined. Heat transfer coefficient determination is problematic because it changes during the reaction. Meindinyo, et al. [44] highlighted this problem in methane hydrate growth estimation based on heat transfer.
- by measuring the difference between the jacket's inlet (Tj, IN) and outlet temperature (Tj, OUT) and the mass flow of the cooling liquid. This method is complicated, however, since the difference between those two temperatures is very small (same order of magnitude of the measurement uncertainty of the sensors).

Adding a thermopile to Tj, IN, and Tj, OUT measurements can improve the second method. A thermopile consists of several thermocouples connected in series [45]. These thermopiles have many applications, such as differential thermal analysis [46, 47] or thermal accelerometers [48]. Hydrate studies use this thermopile measurement for very small-scale calorimeter cells.

This work presents the experimental kinetic of CO_2 hydrate crystallization study by heat balance (using the thermopile approach or classical temperature difference). It compares it to kinetic obtained by mass balance for different propeller types and stirring rates. The novelty of the current approach involves applying the thermopile principle to the temperature difference measurement between the inlet and outlet in a cooling jacket of a stirred tank reactor of 1.4 liters to monitor hydrate crystallization.

2. MATERIAL AND METHOD

This section describes the device, especially the thermopile system, and the protocol used to perform heat balance measurements.

2.1. Raw material specifications

A carbon dioxide gas cylinder of 99.995% (by volume) purity purchased from Linde Gas and ultra-pure water type I, obtained from a Milli-Q® water purification system, were used for the experiments.

2.2. Experimental setup

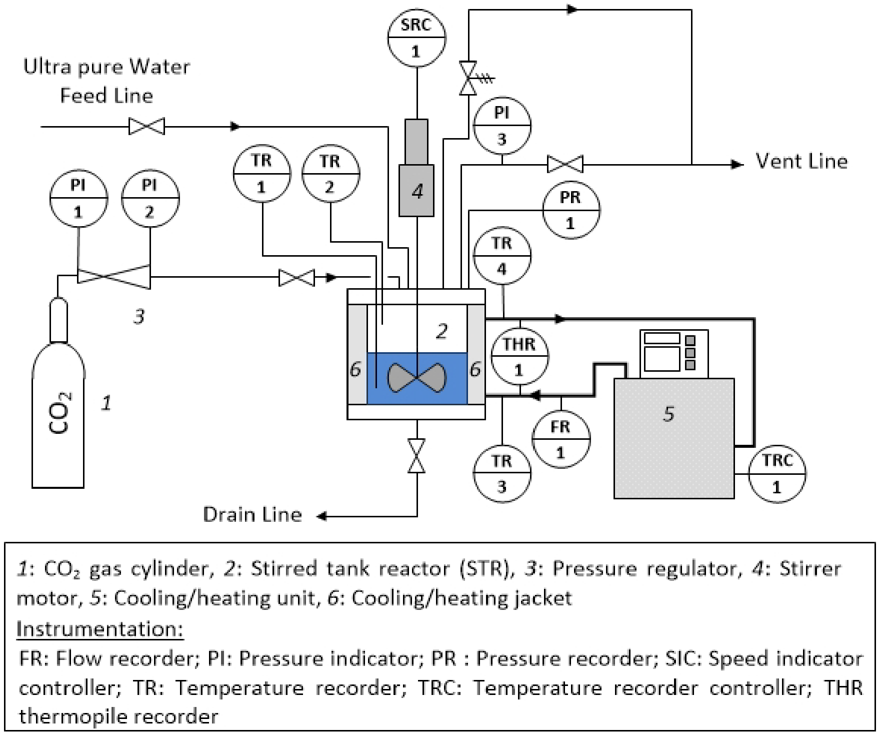

1: CO_2 gas cylinder, *2*: Stirred tank reactor (STR), *3*: Pressure regulator, *4*: Stirrer motor, *5*: Cooling/heating unit, *6*: Cooling/heating jacket

Instrumentation:

FR: Flow recorder; PI: Pressure indicator; PR : Pressure recorder; SIC: Speed indicator controller; TR: Temperature recorder; TRC: Temperature recorder controller; THR thermopile recorder

Figure 1 : Scheme of the experimental setup and instrumentation

This device has been designed and constructed to monitor hydrate formation and dissociation processes by two different methods: measuring the heat flow and measuring the temperature and pressure inside the reactor. It comprises a customized stainless steel reactor with a magnetic drive coupling motor, an external refrigerating unit that cools the fluid flowing in the jacket, and a CO_2 feed bottle. The reactor's maximum operating pressure is 3.8 MPa (pressure safety valve), and its internal volume is $1.4*10^{-3}$ m^3, with an inner diameter of $1.2*10^{-1}$ m.

The magnetic drive coupling motor can be equipped with two types of impeller: a 3-blades propeller and a Dispersimax turbine. A controller can adjust the stirring speed from 100 to 800 rpm.

The reactor's cooling jacket of $0.45 *10^{-3}$ m^3 allows temperature control of reactor temperature with an external heating/ cooling unit (Julabo FP50-HE circulator of 8 L capacity). The temperature stability of the heating/ cooling unit is 0.01°C, the coolant fluid is a mixture of water + mono propylene glycol, and the external insulation of the cooling jacket and the reactor bottom side is a 19 mm thick Armacell sheet. The device is located in a cold room to control the environment's temperature, set at 10 °C for this study.

2.2.1. Instrumentation

Pressure transmitter (PR1) supplied by Keller, calibrated at the laboratory with an uncertainty of 0.1 %, within the range of 0 - 4 MPa, measured the pressure inside the vessel. The CO_2 injection pressure was controlled by a cylinder pressure regulator supplied by Messer with an outlet pressure range of 0 – 10 MPa (PI1&PI2). A pressure indicator (PI3) monitored pressure during the depressurization step. Copper-constantan T-type thermocouples (TR) measured all temperatures, calibrated at the laboratory and with an uncertainty of -/+ 0.2 K within the range of 263.15 - 298.15 K. The position of the thermocouples inside the reactor was such that T_{R1} was in the liquid or slury phase, while T_{R2} was in the vapor phase and it was check before and after each run. A Rosemount 8750W magnetic flowmeter supplied by Emerson Process within a range of 0 – 40 L/hr, measured the flow inside the cooling jacket. The cooling jacket was equipped with a specific sensor (thermopile, see THR in Fig. 1) to perform a direct heat balance on the cooling jacket described hereafter. A Data Acquisition (DAC) system supplied by Agilent, connected to a PC, records temperatures, pressure, flow, and heat balance. The monitoring and recording of all process values (temperature, pressure, flow, heat balance, every 10 s), the control of CO_2 injection, stirring speed and temperature set-point of the heating/cooling unit were done thanks to a VBA in-house software.

2.2.2. Detailed description of the differential temperature measurement method (thermopile)

The thermopile consists of six T-type thermocouples connected in series and distributed as follows (see Fig. 2): the odd thermocouples positions are at the jacket inlet and the even thermocouples are at the jacket outlet.The thermopilee signal was measured between the inlet and outlet side.

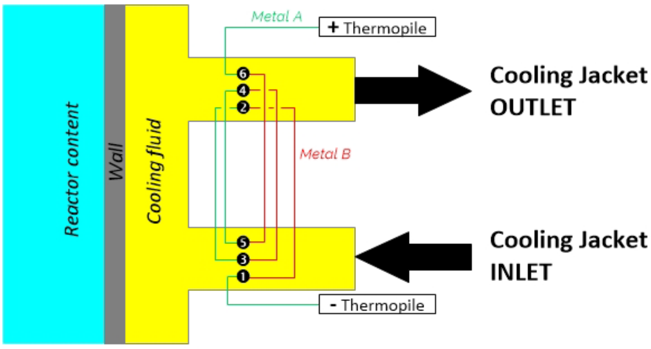

Figure 2: Scheme of thermopile installation

Two other thermocouples are associated with this thermopile to determine temperature at the inlet and outlet of the reactor jacket. The installation of this thermopile is linked to the high uncertainty of the calculated temperature difference, which is the same order of magnitude as the value, often less than 0.1°C. Similarly, the mean and standard deviation were measured and calculated for the inlet and outlet thermocouples and the thermopile measurement. Table 1 presents the standard deviation obtained for each calibration temperature step:

Table 1: Standard deviation of inlet $T_{j,IN}$, outlet $T_{j,OUT}$, calculated difference $T_{j,OUT} - T_{j,IN}$ temperatures, and thermopile signal during calibration

Calibration temperature step		-5 °C	0 °C	5 °C	10 °C	15 °C	25 °C
Standard deviation	T j, OUT (°C)	0.0182	0.0182	0.0153	0.0156	0.0469	0.0182
	T j, IN (°C)	0.0226	0.0219	0.0214	0.0219	0.0564	0.0226
	T j,OUT – T j,IN (°C)	0.0214	0.0176	0.0198	0.0193	0.0201	0.0214
	Thermopile (°C)	0.0035	0.0037	0.0038	0.0040	0.0033	0.0035

The results of Table 1 show that the standard deviation on the outlet-inlet temperature difference is up to four times higher than that of the thermopile.

2.3. Experimental CO_2 hydrates formation protocol

The initial temperature reactor set point was chosen at least 12 °C to avoid the risk of CO_2 hydrate formation during gas injection. The reactor was filled with 0.7 kg of ultrapure water. This study chose this water load to achieve a gas-to-liquid volume ratio of 1:1. After setting the stirring speed (speed set-point of the stirrer ranged between 100 and 760 rpm), the air inside the reactor was removed with a vacuum pump. It allows degassing of any CO_2 naturally dissolved in the water upon contact with the air. Then the reactor was fed with CO_2, filling the vacuum, and part of it was dissolved in water. The amount of gas injected inside the reactor depends on the expected operating conditions (temperature and final hydrates mass fraction). The crystallization process comprises four successive key points marked by the letters A, B, C, and D on Fig. 3.

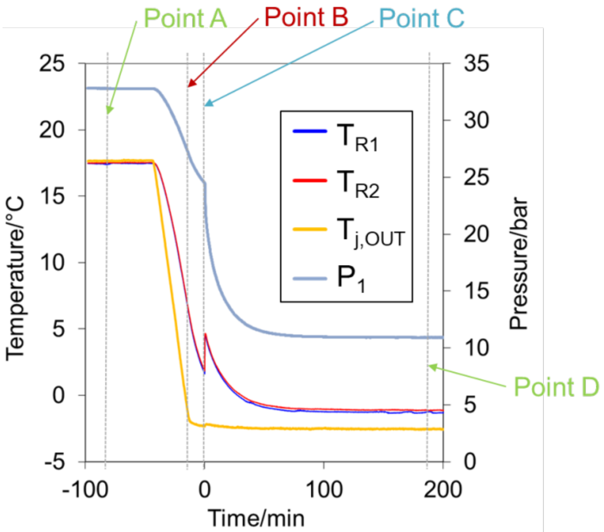

Figure 3 : Pressure inside reactor P_1, temperature inside reactor T_{R1}, T_{R2} and outlet cooling jacket temperature $T_{j,OUT}$ during crystallization process –Point A, B, C and D representation

Point A corresponds to the system's initial state after CO_2 injection and before cooling when the dissolution thermodynamic equilibrium is reached. Point B represents the moment when the system's pressure and temperature have reached thermodynamic conditions that allow hydrate crystallization. However, the system is in a metastable liquid-vapor state between B and C without hydrate crystals. Point C corresponds to the rupture of supercooling. Between C and D, hydrates crystallize. Point D corresponds to the system's final state imposed by the jacket temperature set. In the following results and discussion part, the first experimental result shows those key points.

2.4. Empirical kinetic modeling

The kinetics of crystallization is determined thanks to the thermopile measurement and based on a reactor heat balance in this work. This method was compared with the mass balance method. Those two models were detailed in the following sections.

2.4.1. Description of mass balance model

The mass balance model used in the present work was previously developed by Marinhas et al. (2006) [3]. It is based on CO_2 mass balance in a batch reactor. Initially, before hydrate formation, CO_2 mass balance is given by Eq. 1:

$$n^{i}_{CO_2,tot} = n^{i}_{CO_2,v} + n^{i}_{CO_2,l} = n_{CO_2}(t)$$ **Eq. 1**

With $n_{CO2,tot}$ the total number of CO_2 moles inside the reactor, $n_{CO2,v}$, the number of CO_2 moles in the vapor phase and $n_{CO2,l}$ the number of mole of CO_2 dissolved in the liquid phase.

And in the presence of hydrates:

$$n^{i}_{CO_2,tot} = n_{CO_2,v}(t) + n_{CO_2,l}(t) + n_{CO_2,h}(t)$$ **Eq. 2**

Where:

$$n_{CO_2,h}(t) = n_h(t) \qquad \textbf{Eq. 3}$$

With n_h, the number of moles of crystallized hydrates and $n_{CO2,h}$ is the number of moles of CO_2 involved in the hydrate structure.

Finally, they obtained the mole number of hydrate crystallized inside the reactor only with initial water and CO_2 amount and with pressure and temperature at t time (see Eq. 4).

$$\boldsymbol{n_h(t)} = \frac{\boldsymbol{n_{CO_2,tot} - \sigma_{CO_2,H_2O} * n_{H_2O,tot} - \frac{P_{CO_2}}{ZRT} * \left(V_{tot} - \frac{n_{H_2O,tot} * \left[M_{H_2O} + \sigma_{CO_2,H_2O} * M_{CO_2}\right]}{\rho_l}\right)}}{\boldsymbol{1 - \sigma_{CO_2,H_2O} * nb_H + \frac{P_{CO_2}}{ZRT} * \left(\frac{nb_H * \left[M_{H_2O} + \sigma_{CO_2,H_2O} * M_{CO_2}\right]}{\rho_l} - \frac{M_h}{\rho_h}\right)}} \qquad \textbf{Eq. 4}$$

To use this empirical model, the pressure inside the reactor P_1 and temperature in the slurry phase T_{R1} can be measured. However, assumptions are required to estimate the hydrate mass fraction in the system. The first assumption was made on the hydration number, nb_H, fixed in this case at 7.23, according to the literature [2, 49]. The second assumption was made on the CO_2 amount dissolved in liquid water during the crystallization ($\sigma_{CO2,H2O}$). In the previous work of Marinhas et al. (2006), two theoretical cases, illustrated in Fig. 4, were considered to take into account CO_2 dissolution in liquid during hydrate crystallization:

- Case 1: all phases are in HLV (Hydrate-Liquid-Vapor) thermodynamic equilibrium. In this case, it is assumed that there are no transfer limitations both between the vapor and liquid phases and between liquid and hydrate phases. This case was tested in the early work for convenience, requiring only the knowledge of the experimental temperature and the (known) HLV equilibrium curve to determine vapor and liquid composition. However, it is a strong assumption, particularly regarding the vapor phase, since HLV equilibrium pressure deduced from HLV can differ from experimental pressure.
- Case 2: liquid and vapor phases are in LV (Liquid-Vapor) thermodynamic equilibrium and not with hydrates. In this case, it is assumed that there is still no transfer limitation between vapor and liquid phases, but there is one between hydrate and liquid phases. This case was tested to consider experimental pressure, representative of the vapor phase, contrary to case 1. But the strong assumption is then made on the liquid phase, considering that the transfer of CO_2 at the liquid-vapor interface is much faster than that between the liquid and the hydrates.

In addition, CO_2 dissolution in the liquid phase during hydrate formation was studied by Boufares et al. (2018) in real-time and in-situ by infrared spectroscopy. These results indicate that gas-liquid transfer may be the limiting factor and that a "local" liquid-hydrate equilibrium may occur due to the ability of the hydrate to store a large amount of CO_2 and thus regulate CO_2 dissolution in the liquid phase. A new case, different from cases 1 and 2, can thus be defined as:

- Case 3: liquid and hydrate phases are in HL (Hydrate-Liquid) thermodynamic equilibrium and not with the vapor phase. In this case, it is assumed that there is still no transfer limitation between hydrate and liquid phases, but there is one between vapor and liquid phases. It is thus possible to determine the real-time concentration of CO_2 in the liquid phase simply by following hydrate-liquid equilibrium pressure and temperature data corresponding to solubility data at the theoretical HLV equilibrium curve. A strong assumption is then made on stirring the liquid phase which, must be sufficient to allow a local equilibrium between hydrates and liquid, but limiting to avoid the vapor-liquid equilibrium. A too strong agitation could then lead to case 1.

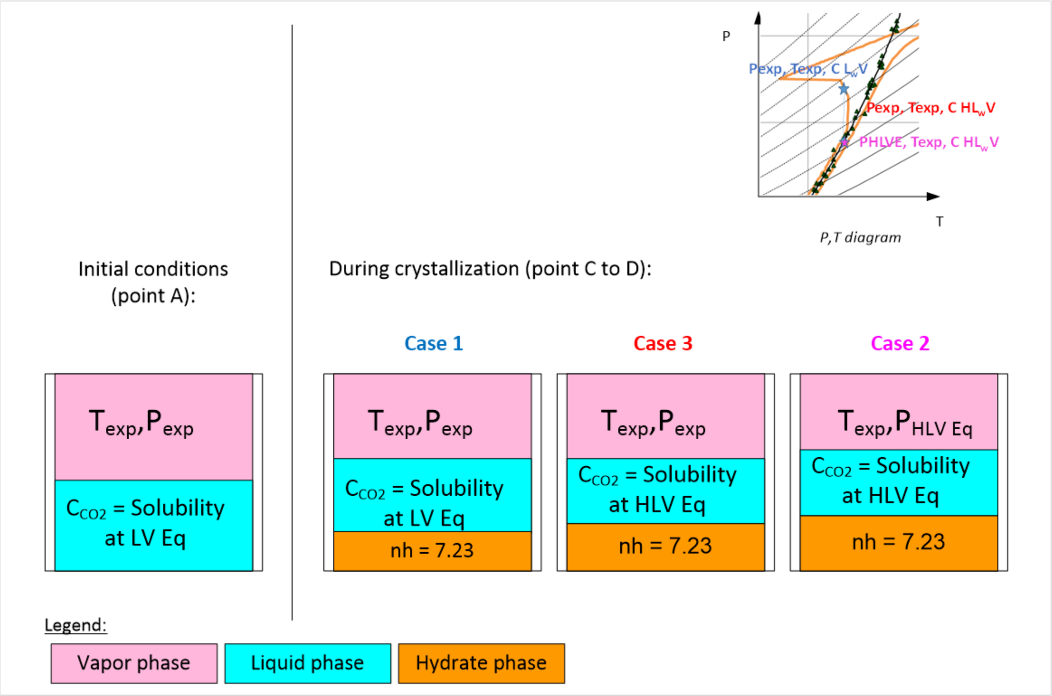

Figure 4 : Different assumptions on the number of mole of CO_2 present in each phase for mass balance in Marinhas model and present work

2.4.2. Description of heat balance model

Fig. 4. shows a scheme of a jacketed reactor with the different heat flows within the reactor during the crystallization of hydrates.

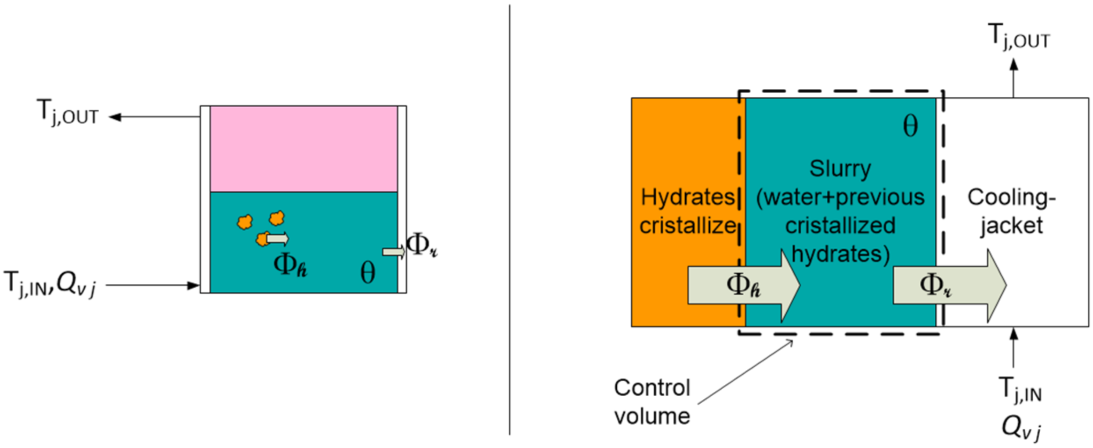

Figure 5 : Heat flux inside the reactor during crystallization

To calculate the hydrate mass fraction, based on thermopile measurement, heat balance on the slurry considered as control volume (see Fig. 4) was written as follows:

$$\begin{aligned}&\textbf{Rate of heat inflow into control volume} - \textbf{Rate of heat outflow from control volume}\\&\quad + \textbf{Rate of heat produced by reaction in control volume}\\&\quad = \textbf{Rate of heat accumulation in control volume}\end{aligned} \qquad \textbf{Eq. 5}$$

In the present case described by Fig. 5, the heat released by the crystallization of new hydrates is considered as heat inflow into the control volume, and no reaction in the control volume is assumed. Another approach could have considered hydrate crystallization as a reaction without any heat inflow into the control volume. This heat released by hydrate crystallization is noted Φ_h. The heat outflow from the control volume is equal to heat removed by the cooling fluid circulating in the cooling jacket, noted Φ_r. The accumulation term corresponds to the sensible heat related to temperature variation of the slurry phase (defined as liquid water phase and already existing hydrate crystals), noted Φ_s . Then Eq. 5 can be expressed as:

$$\Phi_h - \Phi_s = \Phi_r \qquad \text{Eq. 6}$$

Φ_h is a function of the obtained hydrate mass during the considered period, Δm_h, and of the crystallization mass enthalpy of CO_2 hydrates, l_h :

$$\Phi_h = l_h \Delta m_h \qquad \text{Eq. 7}$$

Φ_r is a function of the flow of cooling fluid circulating inside the cooling jacket and the temperature difference measured by the thermopile, $\Delta T_{THERMOPILE}$. The flow of cooling jacket fluid is the product of the density, ρ_j, and the volumetric flow rate of the cooling jacket fluid, Q_{vj}, multiplied by the specific heat capacity, C_{Pj} :

$$\Phi_r = Q_{v_j} \rho_j C_{P_j} \left(T_{j,OUT} - T_{j,IN}\right) \qquad \text{Eq. 8}$$

with $\left(T_{j,OUT} - T_{j,IN}\right) = \Delta T_{THERMOPILE}$

$$\Phi_r = Q_{v_j} \rho_j C_{P_j} \Delta T_{THERMOPILE} = HB \qquad \text{Eq. 9}$$

Φ_s, the accumulation term, depends on the temperature evolution over time of the slurry phase, $\theta(t)$, and is given by the following equation:

$$\Phi_s = m_s C_{P_s} \left(\theta_f - \theta_i\right) \qquad \text{Eq. 10}$$

If the hydrate mass fraction in the slurry is wt_h, and the carrier phase mass fraction is wt_l, then at each moment:

$$wt_h = \frac{m_h}{m_h + m_l} = \frac{m_h}{m_s} = 1 - wt_l \qquad \text{Eq. 11}$$

With m_h, m_l and m_s, representing the quantity of hydrate, liquid and slurry present inside the reactor, respectively. Combining equations 10 and 11 yields the following expression:

$$\Phi_s = m_s\left[wt_h C_{P_h} + (1 - wt_h) C_{P_l}\right]\left(\theta_f - \theta_i\right) \qquad \text{Eq. 12}$$

$$m_s l_h \frac{dwt_h(t)}{dt} = \frac{dHB}{dt} + m_s\left[wt_h(t) C_{P_h} + (1 - wt_h(t)) C_{P_l}\right]\frac{d\theta}{dt} \qquad \text{Eq. 13}$$

Then between t1 and t2 :

$$l_h \Delta wt_h = \frac{HB^{t_1} + HB^{t_2}}{2m_s}(t_2 - t_1) + \left[wt_h{}^{t_1} C_{P_h} + (1 - wt_h{}^{t_1}) C_{P_l}\right](\theta^{t_2} - \theta^{t_1}) \qquad \text{Eq. 14}$$

$$\Delta wt_h = \frac{(HB^{t_1} + HB^{t_2})\,\Delta t + 2m_s\left[wt_h{}^{t_1} C_{P_h} + (1 - wt_h{}^{t_1}) C_{P_l}\right]\Delta\theta}{2 m_s l_h} \qquad \text{Eq. 15}$$

With Δwt_h, the hydrates mass fraction generates between t1 and t2, m_S the slurry quantity at t1, $\Delta\theta$ the temperature variation inside the slurry phase and HB, the rate of heat flow on the cooling jacket side.

3. RESULTS AND DISCUSSION

This section presents the results of CO_2 hydrate crystallization kinetics obtained in the stirred tank reactor. The impact of two operating parameters, stirring speed and stirrer type, on hydrate crystallization enhancement will be studied. For both operating parameters, several characterization results are proposed: experimental temperature and pressure evolution, heat transfer rate from experimental thermopile data, hydrate fraction from heat, and mass balances.

3.1. CO_2 hydrates formation and thermopile measurement

Fig. 6 shows thermopile measurement and calculated temperature difference between the inlet ($T_{j,IN}$) and outlet ($T_{j,OUT}$) of the cooling jacket versus time during a cooling step with hydrate formation. The four key points of the crystallization process, previously described in the “Experimental CO_2 hydrates formation protocol” section, are marked in Fig. 5(a), 6 and, 7 by the letters A, B, C and D. Contrary to the calculated difference, there is no significant fluctuation of the thermopile value during the cooling step between seventy and eighty minutes. Moreover, at point B, the absolute value is 0.2 °C higher with the thermopile signal than with the calculated difference. Even if the value obtained at the supercooling rupture, which marks the beginning of the crystallization (see point C), is similar to the two methods, the signal is less noisy with the thermopile. It is even more striking for stable conditions before cooling and formation (see point A) or after complete crystallization (see point D), where the standard deviation is divided by at least two.

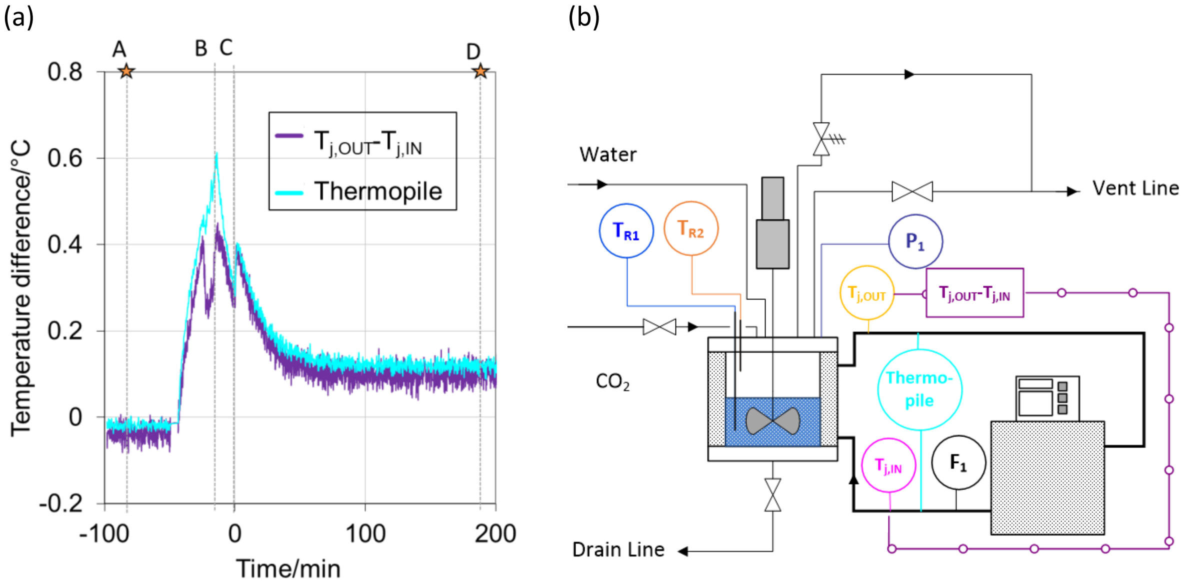

Figure 6 : (a) Temperature difference calculated with $T_{j,OUT}$ - $T_{j,IN}$ (purple curve) and measured by thermopile device (cyan curve) vs. time. (b) Sensors' positions on the device.

Fig. 7 shows the pressure-temperature diagram with thermodynamic equilibrium curves and experimental T_{R1}, P_1. Fig. 8 shows the time evolution of pressure (P_1) and temperatures inside the reactor (T_{R1}, T_{R2}) and the jacket's outlet temperature ($T_{j, OUT}$) for the same test. Reactor contents were cooled when the equilibrium value of CO_2 solubility for the initial pressure and temperature was reached (see point A). The final cooling/heating unit temperature set-point and the cooling rate were monitored and controlled. The beginning of the crystallization (see point C) is linked to a quick pressure drop due to the incorporation of CO_2 in the crystal lattice and an increase of the slurry temperature due to the exothermicity of crystallization. After crystallization occurred, CO_2 hydrate formation was achieved when pressure stabilized with no further drop (see point D in Fig. 6 and Fig. 7).

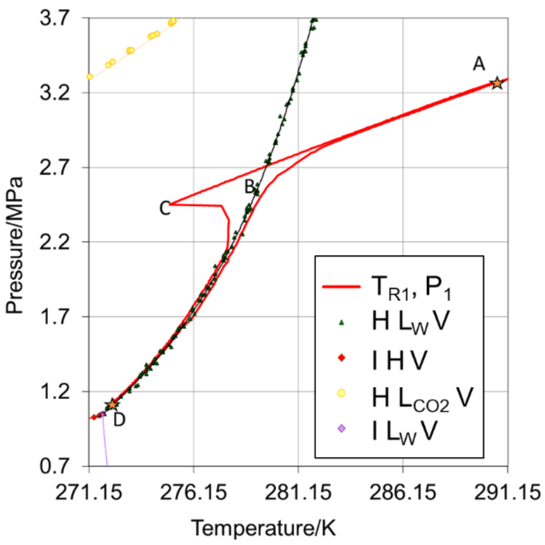

Figure 7 : Pressure-Temperature diagram

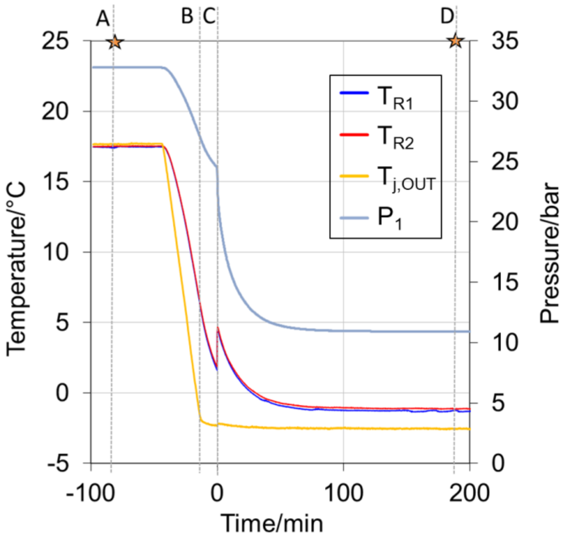

Figure 8 : Pressure and temperature evolution during time

3.2. Stirring speed effect

This section presents the impact of stirring speed on CO_2 hydrate formation kinetics in the tank reactor. Literature reports [28, 34] that increasing stirring speed enhances heat and mass transfer, thus hydrate formation kinetics are governed by these transfers. Four stirring speeds were studied: 100, 420, 610, and 760 RPM. The same initial conditions, same cooling rate, and same cooling jacket inlet final temperature were set and listed in Table 2.

Table 2 : Experimental conditions – stirring speed effect

	Designation	Value	Units
	Stirring impeller	3-blades propeller	-
Environmental conditions	Ambient temperature	10	°C
Initial conditions	Inlet cooling jacket temperature set-point	15	°C
	Pressure inside reactor	27.3	bar abs.
Cooling conditions	Cooling rate	-1.5	°C min^{-1}
Final conditions	Inlet cooling jacket temperature set-point	-0.7	°C

3.2.1. Temperatures and pressure evolution

Fig. 9, Fig. 10, Fig. 11, and Fig. 12 show the evolution of temperature T_{R1} (blue curve), T_{R2} (orange curve), $T_{j,IN}$ (pink curve) and $T_{j,OUT}$ (yellow curve), and pressure P_1 (dark blue curve) during hydrates crystallization for respectively 100, 420, 610 and 760 RPM. The positions of thermocouples and pressure sensors are shown in Fig. 7. On the time axis, t=0 min corresponds to point C (cf. Material and method part), crystallization beginning. For each stirring speed, three runs were performed without showing any significant difference.

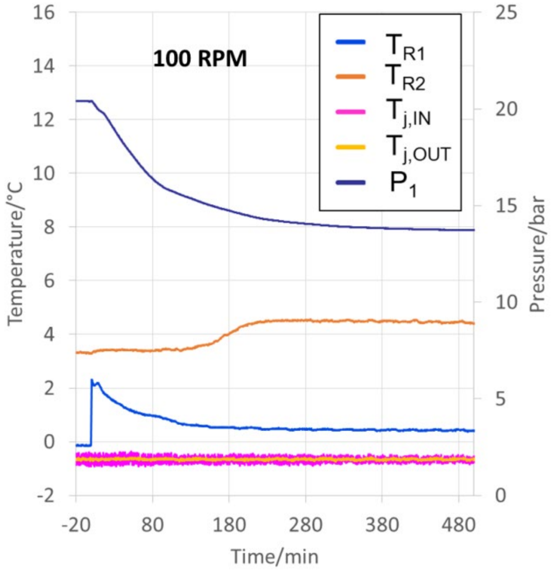

Figure 9 : 100 RPM – Temperatures T_{R1} (inside the slurry), T_{R2} (inside the gas phase), at the inlet and outlet of cooling jacket and pressure P_1 vs. time

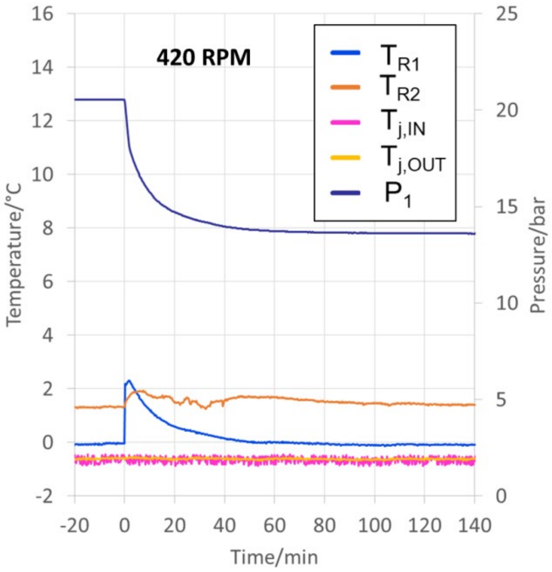

Figure 10 : 420 RPM – Temperatures T_{R1} (inside the slurry), T_{R2} (inside the gas phase), at the inlet and outlet of cooling jacket and pressure P_1 vs. time

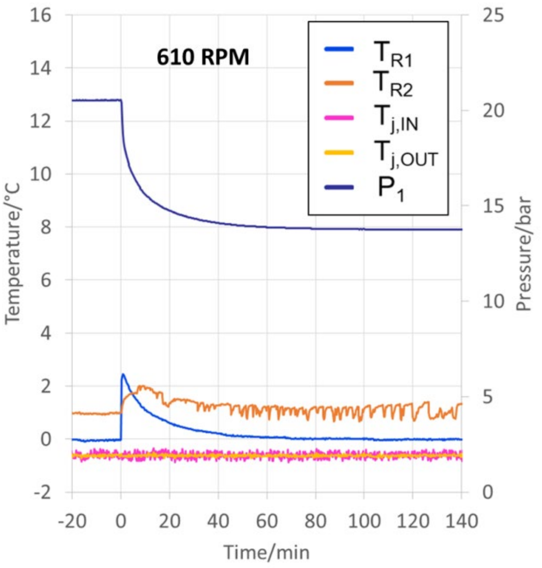

Figure 11 : 610 RPM – Temperatures T_{R1} (inside the slurry), T_{R2} (inside the gas phase), at the inlet and outlet of cooling jacket and pressure P_1 vs. time

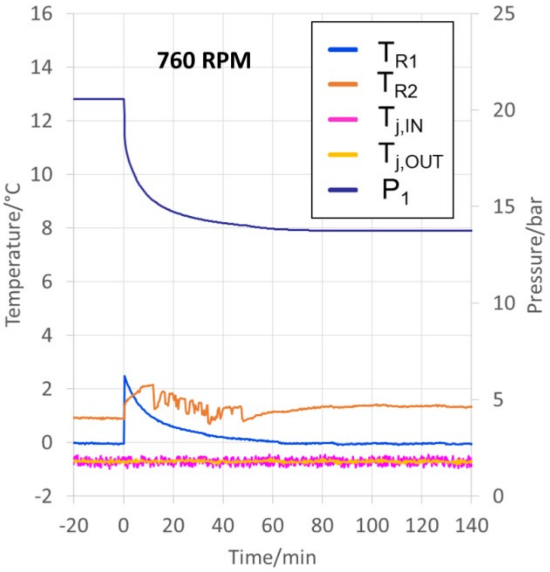

Figure 12 : 760 RPM – Temperatures T_{R1} (inside the slurry), T_{R2} (inside the gas phase), at the inlet and outlet of cooling jacket and pressure P_1 vs. time

In the four figures, crystallization is detected by an increase of the temperature T_{R1} because crystallization is exothermic. This increase is the same for all four tests (about 2.3 °C). It is coupled with a decrease of the pressure P_1 (dark blue curve), particularly in the first moments of the crystallization, due to storing a part of CO_2 in hydrates. No significant difference is observed in the pressure drop for the speeds 420, 610, and 760 RPM. For 100 RPM, the pressure drop is significantly slower, with 380 min required to reach the ending pressure of about 13.8 bar, while 80 min is enough for the three other speeds. The gas phase temperature (T_{R2}) is higher before and after the crystallization at 100 RPM and even reaches the value of 4.5 °C. Note that the final temperature of the slurry (T_{R1}) is higher at 100 RPM than at the other 3 rates, whereas the set temperature of the jacket is the same. This behavior shows that at 100 RPM, the heat transfer is less efficient than at higher speeds.

Fig. 13 shows the evolution of the temperature curves of the slurry phase (T_{R1}) as a function of the system pressure (P_1), represented with HLV equilibrium curves. The 420, 610, and 760 RPM curves have the same shape: before the crystallization, pressure decreases versus temperature following a straight line, and after the supercooling rupture, a curve approaching the HLV equilibrium curve and following it. This kind of curve is rather usual for hydrate crystallization. On the other hand, at 100 RPM, the dissolution is much slower. Indeed, for the same temperature T_{R1}, P_1 at 100RPM is higher than T_{R1}, P_1 at 420RPM, 610RPM or 760RPM. It is because, at 100 RPM, mass and heat transfer are much less efficient. Then, during the induction period, the system reaches the same pressure and temperature conditions before the crystallization begins (see point C). Finally, mass and heat transfers are not so efficient for 100 RPM after hydrate crystallization. The curve shape during crystallization does not follow the equilibrium curve HLV in contrast to stirring speed of 420 RPM or higher. For the same final inlet jacket temperature set-point, the final temperature T_{R1} is slightly different and increases with the speed rate. A slight warming effect can explain this due to the stirring system. The pressure drop during crystallization, especially immediately after supercooling rupture, is higher for 760 RPM than 610 RPM and 420 RPM.

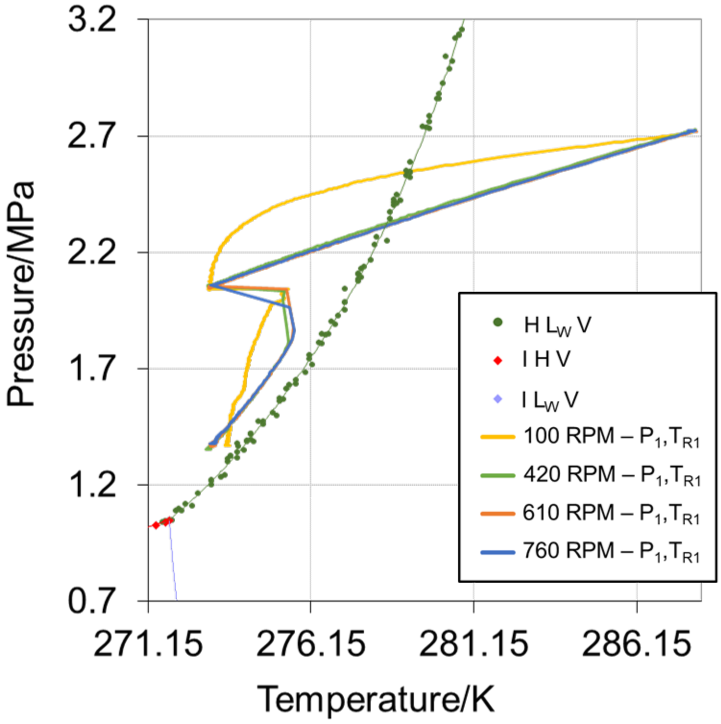

Figure 13 : T,P Diagram for the four stirring speeds (100, 420, 610, and 760 RPM) with a 3-blades propeller

3.2.2. Heat transfer rate

As described in the Material and Method part, evolutions of the heat transfer rate obtained with the thermopile versus time for the four different rates are shown in Fig. 14. The time t = 0 is the beginning of the crystallization for the four curves. The yellow curve represents the test at 100 RPM, the green curve at 420 RPM, the orange curve at 610 RPM, and the blue curve at 760 RPM. It should be noted that the power released in the absence of crystallization (before and after) differs slightly and decreases with the stirring rate increase. It is around 15 W on average for 100 RPM to 7 W on average for 760 RPM. At the supercooling rupture, the power released increases significantly for the three highest rates of about 20 W and decreases to reach a stable heat flux level after 80 min. The heat flux increase for the 100 RPM test is less significant than for higher stirring rates, but the decrease before reaching the stable heat flux level takes longer. The exchanged heat fluxes have the same trend for 420, 610, and 760 RPM, whereas for 100 RPM, the crystallization start seems to release less heat, but the transfer seems longer. Although the thermopile has reduced the noise, the standard deviation on the measurement of heat transfer is +/- 2W. This heat transfer rate curve is then integrated to determine hydrate mass obtained as a function of time (see the heat balance model described above).

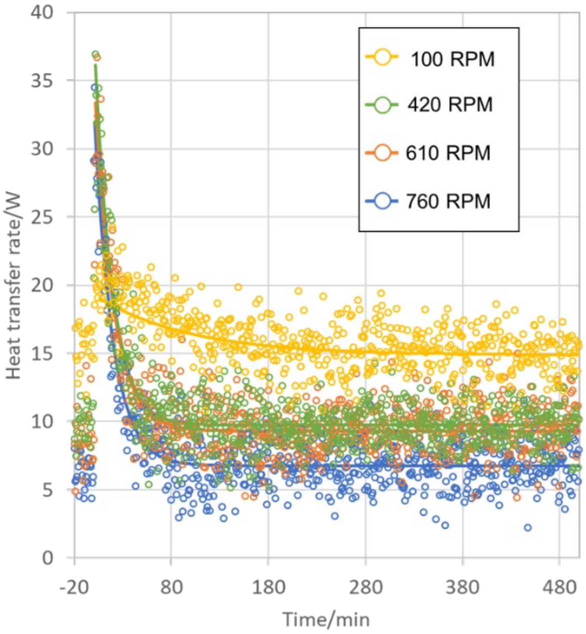

Figure 14 : Heat transfer rate vs. time for 100, 420, 610, and 760 RPM. Dots are experimental data. The solid line is a fit curve.

3.2.3. Hydrate mass fraction obtained with thermopile signal and heat balance

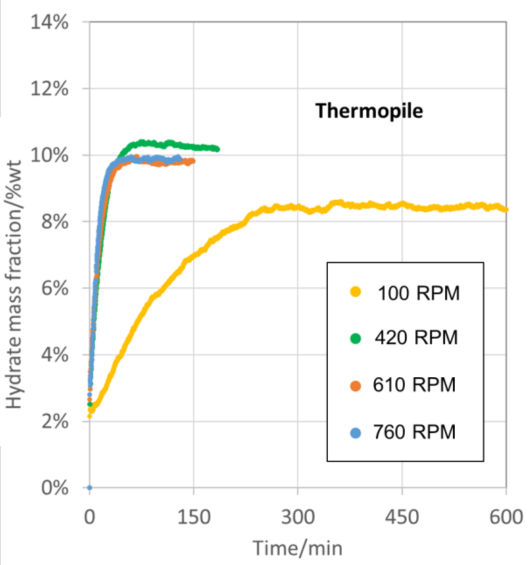

Figure 15 : Hydrate mass fraction vs. time for 100, 420, 610, and 720 RPM obtained with thermopile heat balance.

The evolution of hydrate fraction determined by heat flux is represented in Fig. 15. for the four stirring speeds. The yellow curve represents the test at 100 RPM, the green curve at 420 RPM, the orange curve at 610 RPM, and the blue curve at 760 RPM. The final amount of hydrate deduced by heat balance from the thermopile differs between the four stirring speeds. Instead of converting around 10 % of the slurry into hydrate, as for 420, 610, and 760 RPM, only 8.5 % is converted into hydrate for 100 RPM. The heat balance curves between 420, 610, and 760 RPM are very similar (see

Fig. 14). At 100 RPM, the curve differs from those obtained at higher stirring speeds. Indeed, crystallization kinetic is considerably impacted by the particularly poor heat and mass transfer.

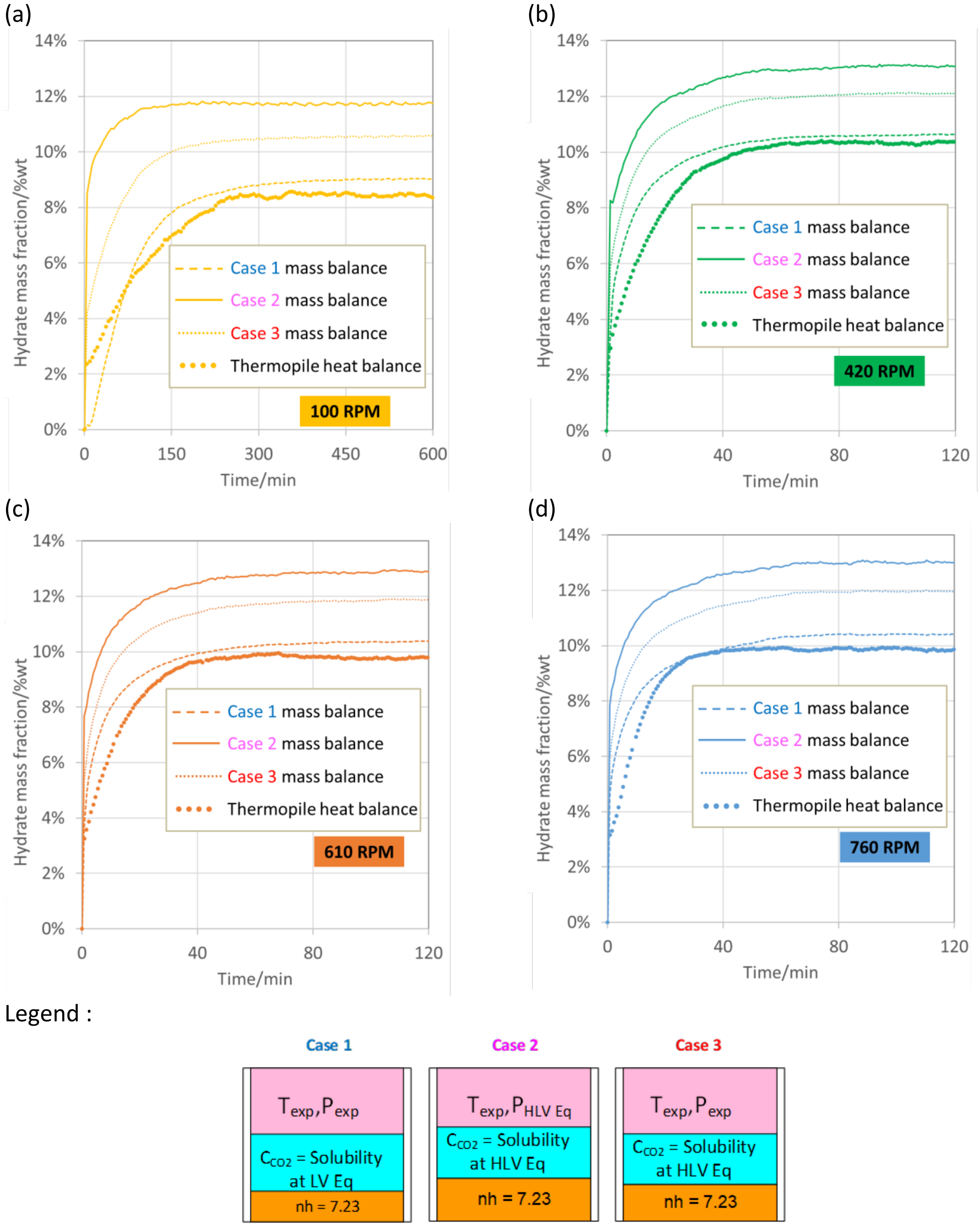

Figure 16 : Comparison between hydrate mass fractions determined with the thermopile heat balance and with the three assumptions cases for mass balance at 100 RPM (15a), 420 RPM (15b), 610 RPM (15c), and 760 RPM (15d)

The comparisons with the mass hydrate fraction calculated from the mass balance method, described by Marinhas, and by heat balance with the thermopile for the four stirring speeds are shown in Fig. 16. First of all, for each experiment at each moment during the crystallization, mass fraction estimated by the mass balance in case 2 are higher than in case 3, which is higher than in case 1 and higher than mass balance obtained thanks to heat balance. The associated assumptions can explain the order of the mass models. Case 1 with pressure, temperature, and solubility at (Texp,

P_{HLV}) considers the lowest pressure in the HLV system and, thus the lowest amount of CO_2 in the vapor and liquid phase, which maximizes the amount of CO_2 in hydrates (batch reactor). On the contrary, Case 2, with pressure, temperature, and solubility at (Texp, Pexp), considers a higher pressure than pressure at HLV, and thus a higher amount of CO_2 in the vapor and liquid phase, which minimizes the amount of CO_2 in hydrates (batch reactor). Case 3 is a combination of the two previous cases, with pressure and temperature at (Texp, Pexp) and solubility at (Texp, P_{HLV}), which explains an intermediate value of hydrate fraction. The mass fractions obtained for the three cases are highly dispersed, even at the final point; this is because experimental pressure is quite far from HLV equilibrium pressure (see Fig. 12). For each experiment, the final hydrate mass fraction obtained with heat transfer measurement seems to be in good agreement with final hydrate mass fraction estimated thanks to the model (and associated assumptions) with Texp, Pexp and CO_2 concentration equal to LV equilibrium solubility (case 2). For the three higher stirring rates, at the beginning of crystallization, the increase of mass fraction according to mass balance (for all cases) was faster than the increase of mass fraction according to heat balance, maybe this can be explained by a delay for the mass transfer due to the thickness of the wall between the reactor and the jacket. Moreover, for 100 RPM, each mass fraction, for each case 1,3, or 2, is lower than for 420, 610, and 760 RPM, even at the final point. This type of stirrer with three inclined blades seems not optimized because even by increasing the stirring speed, the theoretical hydrate amount that could be obtained according to the thermodynamic equilibrium HLV can not be achieved.

3.3. Propeller-type effect

This section presents the impact of the type of impeller on CO_2 hydrate formation kinetics. Literature reports that Dispersimax enhances heat and mass transfer and thus hydrate formation kinetics compared to classic ~~three-pitched blades~~ 3-blade propeller at the same speed rate [28, 34]. For each propeller, three runs were performed without showing any significant difference. Table 3 lists the experimental parameters of the experiments.

Table 3 : Experimental conditions – type of propeller effect

	Designation	Value	Units
	Stirring rate	610	RPM
Environmental conditions	Ambient temperature	10	°C
Initial conditions	Inlet cooling jacket temperature set-point	12	°C
	Pressure inside reactor	30.6	bar abs.
Final conditions	Inlet cooling jacket temperature set-point	-1.3	°C

The hydrate formation protocol is the same as that previously described.

3.3.1. Temperatures and pressure evolution

Fig. 17 and Fig. 18 show the evolution of temperatures T_{R1} (blue curve) in the slurry phase, T_{R2} (orange curve) in the vapor phase, $T_{j,IN}$ (pink curve) at the inlet, and $T_{j,OUT}$ (yellow curve) at the outlet of the cooling-jacket and pressure P_1 (dark blue curve), before and during hydrate crystallization for two different types of stirrer: a Dispersimax (Fig. 16), which corresponds to a Rushton turbine coupled with a gas disperser; the previous used ~~three pitched~~ 3-blade propeller (Fig. 17). On the time axis, t=0 min correspond to point C, crystallization beginning.

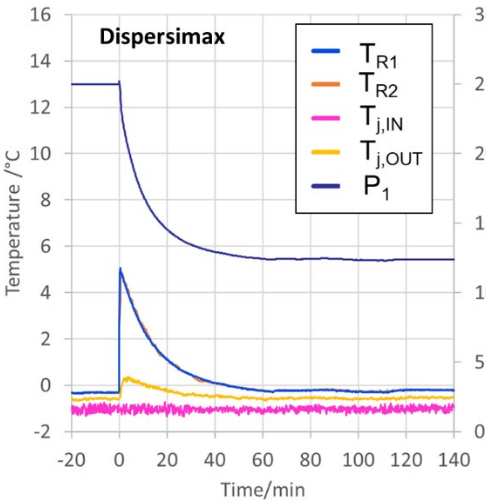

Figure 17 : 610 RPM Dispersimax – Temperatures T_{R1} (inside the slurry), T_{R2} (inside the gas phase), at the inlet and outlet of cooling jacket and pressure P_1 vs. time

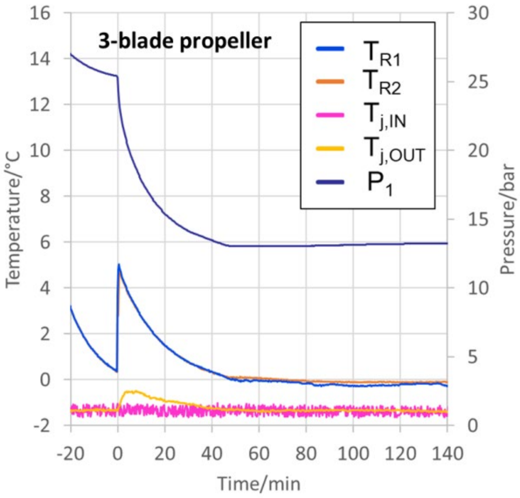

Figure 18 : 610 RPM ~~3 pitched blades~~ 3-blade propeller – Temperatures T_{R1} (inside the slurry), T_{R2} (inside the gas phase), at the inlet and outlet of cooling jacket and pressure P_1 vs. time

Fig. 17 and Fig. 18 show an increase of temperature of 5 °C in the slurry phase (T_{R1}) after the metastability rupture for both stirrers, which is higher than the 2.3 °C observed previously with the ~~three blades~~ 3-blade propeller since the driving force (related to the initial pressure and temperature) in the present experiment is higher than in the previous one. With those new operating conditions, hydrate mass fraction should be around 20 % wt according to mass balance based on HLV equilibrium. As in previous cases with various stirring speeds, hydrate crystallization is linked to the increase in the temperature T_{R1} because crystallization is exothermic and to a decrease in the pressure P_1 (dark blue curve), particularly in the first moments of the crystallization, due to the storage of a part of CO_2 in hydrates. This temperature increase inside the slurry phase (T_{R1}) also corresponds to an increase of the outlet temperature of the jacket ($T_{j,OUT}$) at the beginning of the crystallization, probably related to the amount of heat to be removed by the jacket due to hydrate crystallization. No significant difference is observed on the final point of crystallization except that:

- the final pressure with the ~~three blades pitched~~ 3-blade propeller is a little bit higher than with the Dispersimax.
- the gap between the outlet and inlet jacket temperature is higher with the Dispersimax than with the ~~three pitched blades~~ 3-blade propeller, which seems to attest to a higher heat transfer.

Fig. 19 shows pressure P_1 vs. temperature T_{R1}. The yellow curve corresponds to the Dispersimax run, and the blue curve to the ~~three-pitched blades~~ 3-blade propeller run. The curves have the same shape, with a decrease of pressure versus temperature before the crystallization following a straight line and after the rupture of metastability, a curve approaching the HLV equilibrium curve and following it. At the final point of crystallization, results with Dispersimax are very close to the HLV equilibrium curve, while the results with the 3~~-pitched~~ blade~~s~~ propeller show a slight final increase.

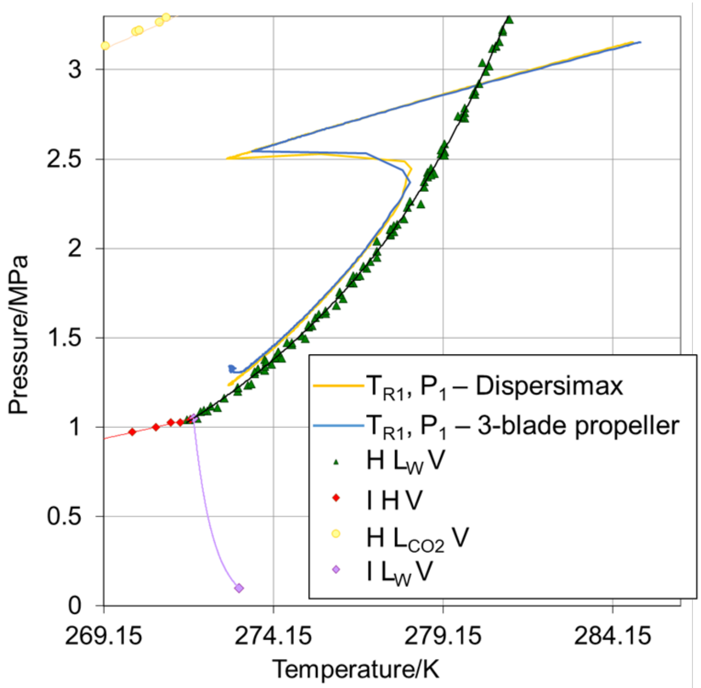

Figure 19 : T,P Diagram for Dispersimax and ~~three pitched blades~~ 3-blade propeller

3.3.2. Heat transfer rate

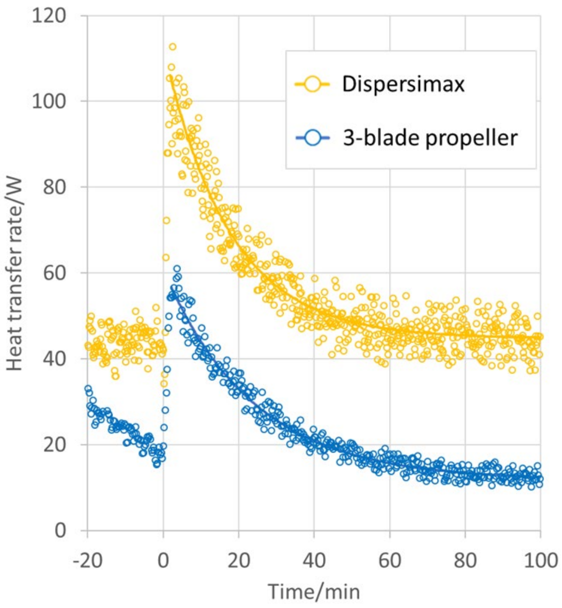

Figure 20 : Heat transfer rate versus time obtained with thermopile signal for Dispersimax and 3-blade propeller at 600 RPM. The solid line is a fit curve.

Fig. 20 represents the heat transfer rate measured thanks to the thermopile for both propellers. The metastability rupture is coupled with a heat transfer reaching 120 W for the Dispersimax compared to 80 W for the 3-~~pitched~~ blade propeller. The heat transfer rate is higher with the Dipersimax before, during, and after crystallization. This impeller probably enhances gas-to-liquid transfer thanks to the gas reinjection by the Venturi effect.

3.3.3. Hydrate mass fractions comparison between thermopile method and mass balance

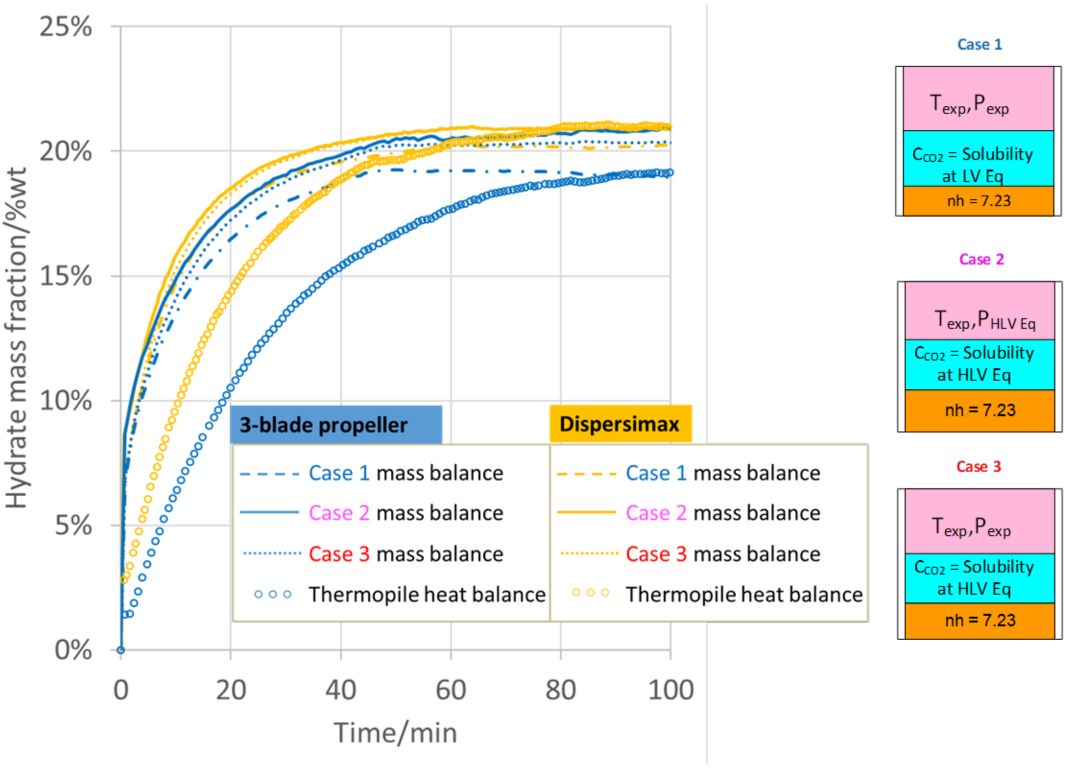

Figure 21 : Hydrate mass fraction (%wt.) for Dispersimax and for 3-blade propeller vs. time, obtained with mass balance and thermopile models

Fig. 21 shows the evolution of hydrate mass fraction obtained with the mass and heat balance (from thermopile signal). Yellow curves represent the hydrate mass fractions for Dispersimax run, and blue curves for the 3-pitched blades propeller run. The gap between mass fractions obtained by the three cases (1, 2, 3) used for mass balance is very small for both impellers, particularly for Dispersimax case. Hydrate formation kinetic and final hydrate mass fraction determined by the heat balance also shows that the Dispersimax enhances it compared to the three-pitched blades propeller. It is in good agreement with mass balance kinetic, especially in case 3. Moreover, in the case of three blade propeller, there is a difference of 1.5 %wt hydrate fraction between mass and heat balances. Finally, kinetics obtained with heat balance is always slower than with mass balance.

4. CONCLUSION

CO_2 hydrates have promising industrial applications as PCMs in secondary refrigeration plants since they crystallize by simple gas injection, have a high fusion enthalpy, and are stable at positive temperatures for refrigeration and air-conditioning applications. However, their kinetic formation could be faster and better controlled. Typically classical methods to characterize hydrate kinetics are based on a mass balance, which depends on rarely experimentally verified assumptions. This work uses a heat flux measurement through the jacket of a pilot-scale reactor with a thermopile to characterize hydrate formation kinetics. The two kinetic parameters of the stirring rate and the type of stirrer were studied. The kinetics obtained by heat balance with the thermopile was compared in each case with the kinetics obtained by mass balance. In all cases, the kinetics determined by heat balance was slower than those estimated by mass balance, but the heat balance method correctly estimates the total amount of hydrates produced. A potential improvement for both these methods could involve the utilization of other sensors to track the evolution of CO_2 concentration in the bulk phase or even the amount of formed hydrates and the particle size distribution of the crystals. For the three-pitched blade stirrer, whatever the stirring rate or the amount of hydrates crystallized, the mass fraction estimated by heat balance with the thermopile was consistently underestimated compared to that obtained by mass balance. For the Dispersimax stirrer, the agreement of final hydrate mass fractions obtained by mass and heat balance is better. Dispersimax's efficiency compared to the ~~three-pitched~~ 3-blade has been confirmed, as well as its limitations, especially for gas-to-liquid transfer with the ~~three-pitched~~ 3-blade stirrer at 100 RPM.

ACKNOWLEDGEMENTS

This work was supported by the French National Research Agency under the program MUSCOFI (ANR-18-CE0-0028), and undertaken in the frame of the US Partnership for International Research and Education program (National Science Foundation Award Number 1743794) and of the French Research Consortium ‘‘GDR-2026 Hydrates de gaz”.

NOMENCLATURE

P	pressure (Pa)	HB	rate of heat flow (J/s)
T	temperature (K)	V	volume (m^3)
n	number of moles (mol)	m	mass (kg)
M	molecular weight (kg/mol)	nb_H	hydrate number (mol_{H2O}/mol_{CO2})
wt	hydrate mass fraction (wt%)	l	molar latent heat (J/mol)
C_p	specific heat capacity (J/kg/K)	Q_v	volumetric flow rate (m^3/s)
Z	gas compressibility factor (-)		
ρ	density (kg/m^3)	Φ	heat flow (J)
θ	temperature inside slurry phase (K)	σ	solubility (mol/mol)
Subscript			
h	hydrate	l	liquid (water phase)
s	Slurry	v	vapor
tot	total		
CO_2	carbon dioxide	H_2O	water
f	Final	i	Intial
r	Reactor	j	cooling jacket
IN	Inlet	OUT	outlet

REFERENCES

[1] L. Fournaison, A. Delahaye, I. Chatti and J.-P. Petitet, CO_2 Hydrates in Refrigeration Processes, Ind. Eng. Chem. Res., 43 (2004) 6521-6526.

[2] S.-P. Kang, H. Lee and B.-J. Ryu, Enthalpies of dissociation of clathrate hydrates of carbon dioxide, nitrogen, (carbon dioxide + nitrogen), and (carbon dioxide + nitrogen + tetrahydrofuran), The Journal of Chemical Thermodynamics, 33(5) (2001) 513-521.

[3] S. Marinhas, A. Delahaye, L. Fournaison, D. Dalmazzone, W. Fürst and J.-P. Petitet, Modelling of the available latent heat of a CO_2 hydrate slurry in an experimental loop applied to secondary refrigeration, Chemical Engineering and Processing: Process Intensification, 45(3) (2006) 184-192.

[4] S. Choi, J. Park and Y. T. Kang, Experimental investigation on CO_2 hydrate formation/dissociation for cold thermal energy harvest and transportation applications, Applied Energy, 242 (2019) 1358-1368.

[5] E. D. Sloan Jr. and C. A. Koh, Clathrate Hydrates of Natural Gases, CRC Press ed., 2007.

[6] J. G. Vlahakis, H.-S. Chen, M. S. Suwandi and A. J. Barduhn, The growth rate of ice crystals: properties of carbon dioxide hydrate, a review of properties of 51 gas hydrates, 830, U. S. Department of the interior, Syracuse, 1972.

[7] M. Wendland, H. Hasse and G. Maurer, Experimental Pressure−Temperature Data on Three- and Four-Phase Equilibria of Fluid, Hydrate, and Ice Phases in the System Carbon Dioxide−Water, Journal of Chemical & Engineering Data, 44(5) (1999) 901-906.

[8] N. Mayoufi, D. Dalmazzone, W. Fürst, L. Elghoul, A. Seguatni, A. Delahaye and L. Fournaison, Phase behaviour of tri-n-butylmethylammonium chloride hydrates in the presence of carbon dioxide, Journal of Thermal Analysis and Calorimetry, 109(1) (2012) 481-486.

[9] J. Oignet, P. Clain, S. Jerbi, A. Delahaye, L. Fournaison and P. Haberschill, Rheological and thermal study of a secondary refrigeration loop with hydrate slurry, Journal, (104) (2013) 8 p.

[10] T. Dufour, Energetic and environmental optimization of storage material introduction in cooling system - Optimisation énergétique et environnementale de l'intégration des matériaux de stockage dans les systèmes de réfrigération, Université Pierre et Marie Curie - Paris VI, 2017.

[11] T. Dufour, H. M. Hoang, J. Oignet, V. Osswald, P. Clain, L. Fournaison and A. Delahaye, Impact of pressure on the dynamic behavior of CO2 hydrate slurry in a stirred tank reactor applied to cold thermal energy storage, Applied Energy, 204 (2017) 641-652.

[12] J. Oignet, H. M. Hoang, V. Osswald, A. Delahaye, L. Fournaison and P. Haberschill, Experimental study of convective heat transfer coefficients of CO2 hydrate slurries in a secondary refrigeration loop, Applied Thermal Engineering, 118 (2017) 630-637.

[13] M. Pons, H.-M. Hoang, T. Dufour, L. Fournaison and A. Delahaye, Energy analysis of two-phase secondary refrigeration in steady-state operation, part 1: Global optimization and leading parameter, Energy, 161 (2018) 1282-1290.

[14] T. Dufour, H. M. Hoang, J. Oignet, V. Osswald, L. Fournaison and A. Delahaye, Experimental and modelling study of energy efficiency of CO2 hydrate slurry in a coil heat exchanger, Applied Energy, 242 (2019) 492-505.

[15] A. Guerra, A. McElligott, C. Yang Du, M. Marić, A. D. Rey and P. Servio, Dynamic viscosity of methane and carbon dioxide hydrate systems from pure water at high-pressure driving forces, Chem. Eng. Sci., 252 (2022).

[16] A. A. A. Majid, D. T. Wu and C. A. Koh, A Perspective on Rheological Studies of Gas Hydrate Slurry Properties, Engineering, 4(3) (2018) 321-329.

[17] S. Jerbi, A. Delahaye, J. Oignet, L. Fournaison and P. Haberschill, Rheological properties of CO_2 hydrate slurry produced in a stirred tank reactor and a secondary refrigeration loop, International Journal of Refrigeration, https://doi.org/10.1016/j.ijrefrig.2012.12.017 (2013) in press.

[18] A. Delahaye, L. Fournaison, S. Jerbi and N. Mayoufi, Rheological Properties of CO_2 Hydrate Slurry Flow in the Presence of Additives, Ind. Eng. Chem. Res., 50(13) (2011) 8344-8353.

[19] A. Delahaye, L. Fournaison, S. Marinhas and M. C. Martínez, Rheological study of CO_2 hydrate slurry in a dynamic loop applied to secondary refrigeration, Chem. Eng. Sci., 63(13) (2008) 3551-3559.

[20] H. Oyama, T. Ebinuma, W. Shimada, S. Takeya, J. Nagao, T. Uchida and H. Narita, An experimental study of gas-hydrate formation by measuring viscosity and infrared spectra, Canadian Journal of Physics, 81(1-2) (2003) 485-492.

[21] V. Andersson and J. S. Gudmundsson, Flow Properties of Hydrate-in-Water Slurries, Annals of the New York Academy of Sciences, 912(1) (2000) 322-329.

[22] J. Oignet, A. Delahaye, J.-P. Torré, C. Dicharry, H. M. Hoang, P. Clain, V. Osswald, Z. Youssef and L. Fournaison, Rheological study of CO2 hydrate slurry in the presence of Sodium Dodecyl Sulfate in a secondary refrigeration loop, Chem. Eng. Sci., 158 (2017) 294-303.

[23] X. Wang, F. Zhang and W. Lipiński, Carbon dioxide hydrates for cold thermal energy storage: A review, Solar Energy, 211 (2020) 11-30.

[24] A. Myerson, Handbook of Industrial Crystallization, Elsevier Science, 2002.

[25] A. Vysniauskas and P. R. Bishnoi, A kinetic study of methane hydrate formation, Chem. Eng. Sci., 38(7) (1983) 1061.

[26] A. Vysniauskas and P. R. Bishnoi, Kinetics of ethane hydrate formation, Chem. Eng. Sci., 40(2) (1985) 299-303.

[27] P. Englezos, N. Kalogerakis, P. D. Dholabhai and P. R. Bishnoi, Kinetics of formation of methane and ethane gas hydrates, Chem. Eng. Sci., 42(11) (1987) 2647-2658.

[28] S. Douïeb, L. Fradette, F. Bertrand and B. Haut, Impact of the fluid flow conditions on the formation rate of carbon dioxide hydrates in a semi-batch stirred tank reactor, AIChE Journal, 61(12) (2015) 4387-4401.

[29] M. B. Malegaonkar, P. D. Dholabhai and P. R. Bishnoi, Kinetics of carbon dioxide and methane hydrate formation, Canadian Journal of Chemical Engineering, 75(6) (1997) 1090-1099.

[30] Y. He, E. S. J. Rudolph, P. L. J. Zitha and M. Golombok, Kinetics of CO2 and methane hydrate formation: An experimental analysis in the bulk phase, Fuel, 90(1) (2011) 272-279.

[31] K. Ohgaki, Y. Makihara and K. Takano, Formation of CO2 Hydrate in Pure and Sea Waters, Journal of Chemical Engineering of Japan, 26 (1993) 558-564.

[32] K. A. Udachin, C. I. Ratcliffe and J. A. Ripmeester, Structure, composition, and thermal expansion of CO_2 hydrate from single crystal X-ray diffraction measurements, The Journal of Physical Chemistry B, 105(19) (2001) 4200-4204.

[33] W. Ou, W. Lu, K. Qu, L. Geng and I. M. Chou, In situ Raman spectroscopic investigation of flux-controlled crystal growth under high pressure: A case study of carbon dioxide hydrate growth in aqueous solution, International Journal of Heat and Mass Transfer, 101 (2016) 834-843.

[34] A. Boufares, E. Provost, D. Dalmazzone, V. Osswald, P. Clain, A. Delahaye and L. Fournaison, Kinetic study of CO_2 hydrates crystallization: Characterization using FTIR/ATR spectroscopy and contribution modeling of equilibrium/non-equilibrium phase-behavior, Chem. Eng. Sci., 192 (2018) 371-379.

[35] M. A. Clarke and P. R. Bishnoi, Determination of the intrinsic kinetics of CO_2 gas hydrate formation using in situ particle size analysis, Chem. Eng. Sci., 60(3) (2005) 695-709.

[36] P. Clain, F. T. Ndoye, A. Delahaye, L. Fournaison, W. Lin and D. Dalmazzone, Particle size distribution of TBPB hydrates by focused beam reflectance measurement (FBRM) for secondary refrigeration application, International Journal of Refrigeration, 50 (2015) 19-31.

[37] H. Kim, J. Zheng, Z. Yin, S. Kumar, J. Tee, Y. Seo and P. Linga, An electrical resistivity-based method for measuring semi-clathrate hydrate formation kinetics: Application for cold storage and transport, Applied Energy, 308 (2022) 118397.

[38] X. Liu, Y. Li, G. J. Chen, D. Y. Chen, B. Sun and Z. Yin, Coupling Amino Acid with THF for the Synergistic Promotion of CO2 Hydrate Micro Kinetics: Implication for Hydrate-Based CO2 Sequestration, ACS Sustainable Chem. Eng., 11(15) (2023) 6057-6069.

[39] M. Brown, Introduction to Thermal Analysis: Techniques and Applications, 2001.

[40] D. Dalmazzone, N. Hamed and C. Dalmazzone, DSC measurements and modelling of the kinetics of methane hydrate formation in water-in-oil emulsion, Chem. Eng. Sci., 64(9) (2009) 2020-2026.

[41] P. Clain, V. Osswald, O. Spiga, A. Delahaye and L. Fournaison, A new formation kinetic study method of TBPB and CO_2 hydrates based on DTA, Journal, (2015).

[42] N. S. Murthy, Chapter 3 - Experimental Techniques for Understanding Polymer Crystallization, in: S. Thomas, M. Arif P, E. B. Gowd and N. Kalarikkal (Eds.) Crystallization in Multiphase Polymer Systems, Elsevier, 2018, pp. 49-72.
[43] Z. Yin, G. Moridis and P. Linga, On the importance of phase saturation heterogeneity in the analysis of laboratory studies of hydrate dissociation, Applied Energy, 255 (2019) 113861.
[44] R.-E. T. Meindinyo, T. M. Svartaas, T. N. Nordbø and R. Bøe, Gas Hydrate Growth Estimation Based on Heat Transfer, Energy & Fuels, 29(2) (2015) 587-594.
[45] N. Lior, Chapter 1.2 Measurement of small temperature and pressure differences, Desalination, 59 (1986) 19-60.
[46] J. W. Schaefer and R. L. Danley, Thermopile differential thermal analysis sensor, in, 1992.
[47] R. A. Secco, High pressure DSC signal amplification using thermopiles, AIP Conference Proceedings, 309(1) (1994) 1691-1694.
[48] R. Mukherjee, J. Basu, P. Mandal and P. Guha, A Review of Micromachined Thermal Accelerometers, Journal of Micromechanics and Microengineering, 27 (2017).
[49] P. B. Gjerstad, Enthalpies of CH_4 and CO_2 Hydrate Formation and Dissociation Using Residual Thermodynamics, The University of Bergen, 2019.